





The 28 January 2020, Mw 7.7, Cayman Trough / Oriente Fault, Supershear Earthquake Rupture

Eric Calais ^{*1,2}, Bertrand Delouis ², Jean-Paul Ampuero ², Han Bao ³, Françoise Courboux ², Anne Deschamps ², Bernard de Lépinay ², Tony Monfret ^{2,10}, Lingsen Meng ³, Liuwei Xu ³, Charles deMets ⁴, O'Leary Gonzalez ⁵, Enrique Arango-Arias ⁵, Bladimir Moreno ⁵, Raul Palau ⁵, Manuel Cutie ⁵, Eduardo Diez ⁵, Ernesto Rodríguez Roche⁶, Jorge Garcia⁶, Enrique Castellanos ⁷, Steeve Symithe ⁸, Paul Williams⁹

¹Université PSL, École Normale Supérieure, CNRS UMR 8538, Paris, France, ²Université Côte d'Azur, Observatoire de la Côte d'Azur, CNRS, IRD, Géoazur, Valbonne, France, ³Department of Earth, Planetary and Space Sciences, University of California, Los Angeles, CA, USA, ⁴Department of Geoscience, University of Wisconsin, Madison, USA, ⁵Centro Nacional de Investigaciones Sismológicas (CENAI), Santiago de Cuba, Cuba, ⁶Grupo Empresarial GEOCUBA, Havana, Cuba, ⁷Ministerio de Energía y Minas (MINEM), Havana, Cuba, ⁸Université d'État d'Haïti, Faculté des Sciences, Unité de Recherche en Géosciences, Port-au-Prince, Haïti, ⁹Earthquake Unit of the University of West Indies Mona Campus, Jamaica, ¹⁰Barcelona Center for Subsurface Imaging, Institut de Ciències del Mar (ICM), CSIC, Barcelona, Spain

Author contributions: *Conceptualization:* Calais, Ampuero, Delouis, Bao. *Data Curation:* Cutie, Diez, Roche, Garcia, Castellanos, Williams. *Formal Analysis:* Delouis, Bao, Ampuero. *Funding Acquisition:* Calais, deMets. *Investigation:* Courboux, Deschamps, de Lépinay, Monfret, Meng, Xu, deMets, Gonzalez, Arango-Arias, Moreno, Palau. *Writing – Original Draft Preparation:* Calais, Delouis, Bao, Ampuero, Moreno. *Writing – Review & Editing:* All coauthors.

Abstract On 28 January 2020, an earthquake of moment magnitude 7.7 ruptured the Oriente transform fault along the northern edge of the Cayman Trough, west of Cuba. It is the largest magnitude strike-slip event of the instrumental seismology era along the northern Caribbean plate boundary. We use local, regional, and global seismic waveforms and coseismic geodetic offsets, to produce high-resolution rupture models for both the low-frequency (~ 0.02 Hz) and high-frequency (~ 1 Hz) components of the rupture using a finite fault kinematic inversion and back-projection imaging, respectively. We document a rupture that propagated predominantly unilaterally westward, with an initial phase at subshear speed for 20–30 s and over 40 to 50 km, followed by an acceleration to supershear speed that persisted to the western end of the rupture, for 40 s and over about 200 km. Supershear rupture speed is consistent with low aftershock production in numbers and moment release. The rupture followed a very linear, unsegmented portion of the Oriente fault that had not experienced significant seismic activity for at least a century. Observational evidence and models indicate that the 28 January 2020, M_w 7.7 earthquake, supershear over most of its length, had a smooth rupture process along a simple linear fault segment where earthquake nucleation is infrequent and interseismic locking depth shallow. These two characteristics, which translate into the accumulation of large amounts of interseismic stress, may explain this unusually large supershear event.

Production Editor:
Andrea Llenos
Handling Editor:
Meng (Matt) Wei
Copy & Layout Editor:
Anant Hariharan

Received:
March 19th, 2025
Accepted:
July 21th, 2025
Published:
August 31st, 2025

1 Introduction

The 28 January 2020, M_w 7.7 earthquake along the northern edge of the Cayman Trough west of Cuba (Figure 1) is the largest magnitude strike-slip event recorded in the instrumental seismology era along the northern Caribbean transcurrent plate boundary. It surpasses the 4 February 1976, M_s 7.5 Guatemala earthquake along the Motagua fault (Plafker, 1976), as well as the more recent 2009, M_w 7.3 (Graham et al., 2012), 2018, M_w 7.5 (Cheng and Wang, 2020), and 2025, M_w 7.6 (USGS, 2025) events on the Swan fault. Its estimated rupture length is approximately 300 km, with a downdip width of 20 km – hence involving a complete rupture of the crust – a coseismic slip reaching 4 m, and a moment magnitude reported between 7.7 (USGS, 2020) and 7.8 (GEOSCOPE, 2021). The source mechanism is predominantly strike-slip, with one nodal plane parallel to the plate boundary strike. Initial finite fault modeling

(USGS, 2020) indicates that this event likely ruptured the Oriente fault (Figure 2), a major left-lateral strike-slip fault that delineates the shallow, locally emerging, Cayman Ridge from the 5000–7000 m–deep Cayman Through (Bowin, 1968; Perfit and Heezen, 1978). This is consistent with most other focal mechanisms on the Oriente fault from its intersection with the mid-Cayman spreading center, to the western end of eastern Cuba (Perrot et al., 1997; vanDusen and Doser, 2000; Moreno et al., 2002). Interestingly, this earthquake ruptured a segment of the Oriente fault that had not experienced significant seismic activity for at least one century, as shown in Figure 1B by the lack of $M > 6$ earthquakes along its rupture.

Tadapansawut et al. (2020), through an analysis of teleseismic P-waveforms, contend that this event had a complex rupture geometry and included portions occurring at supershear velocities. In a global survey of supershear earthquakes between 2000 and 2020, Bao et al. (2022) identified this earthquake as supershear over most of its rupture length using two independent

*Corresponding author: eric.calais@ens.fr

methods: teleseismic back-projection imaging and far-field Rayleigh Mach wave analysis. The event triggered a small but region-wide tsunami, detected at tide gauges on Grand Cayman Island, as well as at the northeast tip of the Yucatan peninsula, about 500 km from the rupture, caused by the combination of small coseismic reverse faulting and submarine landsliding near the Cayman Islands, according to Xu et al. (2022).

In this study, we use local, regional, and global seismic waveforms, along with local and regional coseismic geodetic offsets, to determine the rupture mechanism of the 28 January 2020 Cayman Trough / Oriente Fault earthquake. We perform a joint inversion of seismic and space geodetic data to derive a finite-fault solution, employing the methodology outlined by Delouis et al. (2002). We also image the rupture at high frequency using the MUSIC back-projection technique (Meng et al., 2012), incorporating slowness calibration through dense seismic networks located in Alaska and Europe. By leveraging this extensive dataset, we produce high-resolution rupture models for both the high-frequency (~ 1 Hz) and low-frequency (~ 0.02 Hz) components of the rupture. Collectively, our data and models indicate a rupture that propagates predominantly unilaterally westward and transitions from sub-shear to supershear after about 20 seconds.

2 Seismotectonic setting

The Caribbean region and Central America constitute a small lithospheric plate situated between the large North and South American plates (Figure 1), currently moving east relative to both at a rate of 18 to 20 mm/year (deMets et al., 2000; Symithe et al., 2015). This study focuses on the central section of the northern boundary of the Caribbean plate, which was the locus of the M_w 7.7, 28 January 2020 earthquake (Figure 1). In this area, the Caribbean–North America plate boundary is marked by the Cayman Trough (Bowin, 1968; Perfit and Heezen, 1978; Holcombe and Sharman, 1983), a pull-apart basin bounded to the north by the Oriente fault and to the south by the Swan, Walton and Enriquillo–Plantain Garden faults, from west to east (Mann and Burke, 1984). The Cayman Trough has been undergoing accretion of oceanic crust for approximately 45–50 million years at the ultra-slow mid-Cayman Spreading Center (MCSC) (Leroy et al., 2000; Hayman et al., 2011). Seismic, gravity, and magnetic data indicate a 3–6 km-thick oceanic crust in the central portion of the Cayman Trough, juxtaposed to the west and east with a 20–30 km-thick extended island arc crust (Rosencrantz et al., 1988; Leroy et al., 1996; tenBrink et al., 2002; Peirce et al., 2022; Moreno et al., 2023).

To the south and west, the MCSC connects to the left-lateral Swan fault (Rosencrantz and Mann, 1991), which was the locus of an M_w 7.3 earthquake on January 10, 2010 (Graham et al., 2012). To the north and east, it connects with the Oriente fault (Mann and Burke, 1984), where earthquake focal mechanisms indicate pure left-lateral strike-slip motion from the MCSC to the southern margin of Cuba (Perrot et al., 1997). At this location, the fault trace slightly changes direction, coinci-

dent with transpressional structures along the southern margin of eastern Cuba (Calais and de Lépinay, 1991). There, earthquake focal mechanisms show a combination of thrust and strike-slip faulting, strikingly different from the uniform population of pure strike-slip faulting events observed to the east along the Cayman Ridge segment of the Oriente fault (Calais et al., 1998; vanDusen and Doser, 2000; Moreno et al., 2002). Kinematic models derived from GPS measurements throughout the Caribbean predict a slip rate of approximately 10 mm/year on the Oriente fault (Benford et al., 2012; Symithe et al., 2015). In a recent study based on GPS data in Cuba and the Cayman Islands, Calais et al. (2023) argue that the Oriente fault locking depth varies from about 25 km along the southern margin of eastern Cuba to less than 5 km along the Cayman Ridge segment of the Oriente fault.

The bathymetry of the segment of the Oriente fault that ruptured during the 28 January 2020 earthquake is illustrated in Figure 2. The Oriente fault follows the base of a major submarine escarpment that separates the Cayman Ridge and its associated islands from the Cayman Trough, with an elevation differential slightly exceeding 7,000 m. The south-facing slope of the Cayman Ridge exhibits irregularities, with a series of slope-parallel flats and slope-normal valleys. Dredging along the Cayman Ridge slope brought metamorphic and plutonic rocks from the late Cretaceous to the Paleogene, along with volcanic and volcanoclastic rocks of undetermined age (Perfit and Heezen, 1978). These materials bear resemblance to those found on land within the Northern Caribbean region, where they delineate a Cretaceous to Paleocene orogenic belt commonly referred to as the “Great Arc of the Caribbean” (Burke, 1988).

The toe of the Cayman Ridge escarpment is characterized by a narrow, flat-bottom basin approximately 20 km in width and 200 km in length (Figure 2), continuous to the east with the Cabo Cruz basin and the Oriente Deep (Calais and de Lépinay, 1991). It was identified early on by Taber (1922) as “a series of elongated depressions containing four of the deepest soundings obtained in these waters”, hence deeper than the floor of the Cayman Trough, which was then named “Bartlett Trough”. Modern bathymetry indeed shows that this elongated basin is bounded to the south by a 2,000 m-high north-facing escarpment that separates it from the floor of the oceanic portion of the Cayman Trough. This narrow, flat-bottom basin is likely filled with recent sediments derived from both the Cayman Ridge to the north and the Cayman Trough to the south. The basin floor exhibits a series of narrow ridges aligned parallel to its strike, each 2–5 km-wide and 30–50 km-long, rising up to 300 m above the basin floor, and showing a left-stepping *en échelon* configuration (Figure 2). These structures are similar to pressure ridges formed along left-lateral strike-slip faults (Wilcox et al., 1973; Sylvester, 1988). They likely materialize the current active surface trace of the Oriente fault, which is therefore linear and unsegmented along this 200 km-long Cayman Ridge segment of the plate boundary.

To the east, this basin connects to the Cabo Cruz pull-apart basin (Calais and de Lépinay, 1991), which was

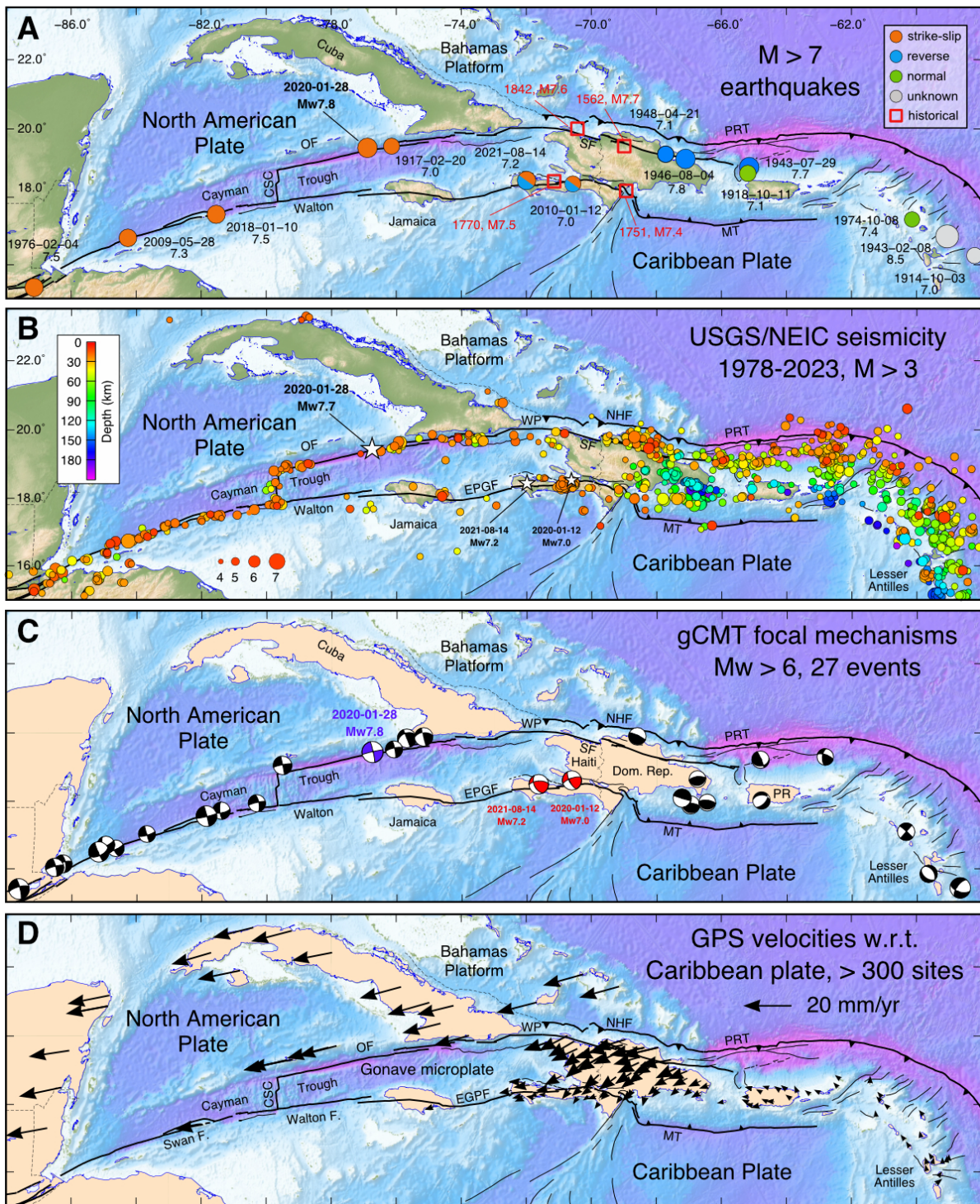


Figure 1 Seismotectonic and plate kinematic setting of the Northern Caribbean plate boundary. A: Large ($M > 7$) earthquakes in the Northern Caribbean. The 28 January 2020, M_w 7.7 Cayman Trough earthquake is the largest magnitude strike-slip event of the instrumental seismology era in this region. Historical earthquakes are from [tenBrink et al. \(2011\)](#) and [Hough et al. \(2023\)](#). B: 1978 to 2023 seismicity along the Northern Caribbean plate boundary according to the USGS/NEIC catalog, with magnitude greater than 3. Note the earthquake gap along the Oriente Fault from the epicenter of the January 28 earthquake westward. C: source mechanisms for earthquakes with $M_w > 6$, according to the gCMT catalog. Note the transition from shallow strike-slip events and fault-parallel kinematics west of $\sim 74^\circ\text{W}$, to a combination of strike-slip and plate-boundary-shortening east of that longitude. D: GNSS-derived velocities with respect to the Caribbean plate at selected sites, from [Calais et al. \(2023\)](#) OF: Oriente fault, WP: Windward Passage, SF: Septentrional fault, EPG: Enriquillo-Plantain Garden fault, NHF: North Hispaniola fault, PRT: Puerto Rico trench, MT: Muertos trench, CSC: Cayman spreading center, PR: Puerto Rico.

the epicenter of a M_w 6.9 earthquake in 1992 ([Perrot et al., 1997](#)). To the west, it bifurcates into two narrow trenches on their side of an elongated ridge ([Peirce](#)

[et al., 2022](#)). The trench bordering this ridge on the south side extends approximately 100 km westward to connect with the MCSC and likely represents the west-

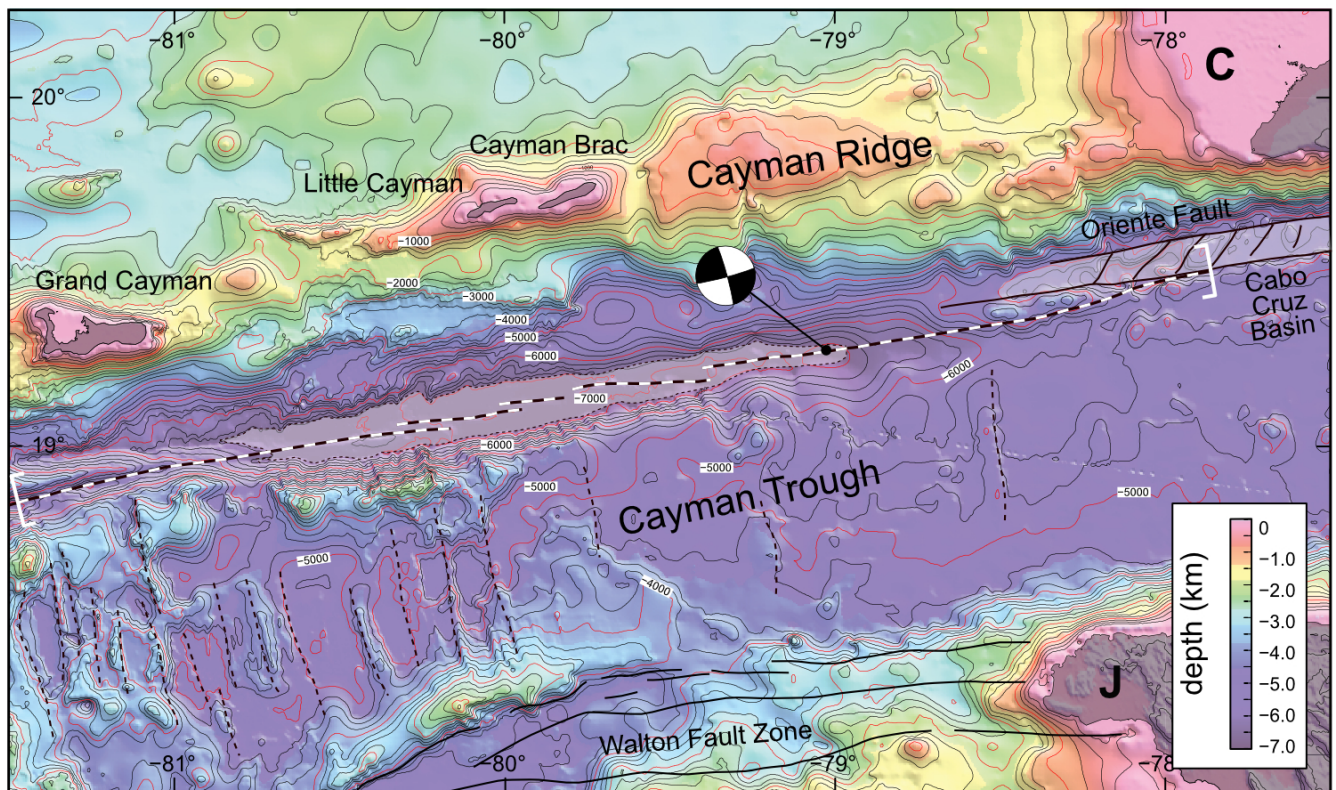


Figure 2 Bathymetry of the segment of the Oriente fault that ruptured during the 28 January 2020, earthquake (GEBCO, 2024). The active trace of the Oriente fault is marked by narrow en échelon ridges that cut through the center of a narrow, about 7,000 m deep, flat-bottom basin along the toe of the Cayman Ridge. It connects to the east with the Cabo Cruz pull-apart basin. The fault segment used in the kinematic slip inversion is bounded by two white brackets. The earthquake source mechanism (USGS) and its hypocenter surface projection as determined by the slip inversion are indicated.

ward continuation of the active trace of the Oriente fault. Dredging along the north facing scarp that delineates the southern boundary of this basin yielded samples of serpentine and serpentinized peridotites from the oceanic portion of the Cayman Trough (Perfit and Heezen, 1978).

3 Methods

3.1 GPS data analysis and coseismic offsets

The GPS data used here to determine coseismic offsets come from (1) open-access, continuous Caribbean stations part of the IGS (Johnston et al., 2017) and CocosNet networks (Braun et al., 2012), (2) restricted-access, continuous GPS data in Cuba and Jamaica, and (3) campaign GPS data from Cuba and Jamaica. Campaign post-earthquake GPS data were acquired in Jamaica on March 13–19, 2020. In Cuba, they were acquired in several batches spanning April to December 2000, as logistical conditions did not allow for early measurements at all the sites. We processed Caribbean-wide and Cuba data using the GAMIT-GLOBK software (Herring et al., 2015) and Jamaica data using the GIPSY-OASIS software (Zumberge et al., 2007) following well-established procedures described, for instance, in Symithe et al. (2015) and Ellis et al. (2018).

We calculate coseismic offsets at continuous stations from the difference in site coordinates by averaging their positions for five days before the earthquake and

five days after it, as illustrated in Supplementary Figure 1 (bottom). This is meant to minimize the effect of postseismic deformation, while averaging position over a long enough time interval to gain precision. For campaign sites, we use two approaches. In Jamaica, where the campaign sites were occupied 4 to 8 times over the 10 to 19 years preceding the earthquake, we compute pre-earthquake site positions by a least-squares fit of a slope to the pre-earthquake data that we extrapolate up to the date of the event. In Cuba, as campaign sites have at most two pre-earthquake observation epochs, estimating an interseismic velocity would lead to significant errors in the calculation of coseismic offsets. We therefore use interseismic velocities from the kinematic block model of Symithe et al. (2015), which accounts for plate and block rigid rotations and interseismic strain accumulation on locked faults. We fit this slope to pre-earthquake data and extrapolate it up to the date of the event to obtain pre-earthquake site positions. In Cuba and Jamaica, we compute post-earthquake site positions by fitting interseismic velocities – observed for Jamaica, derived from a kinematic model for Cuba – to post-earthquake data and interpolating the slope back to the date of the earthquake. We calculate the coseismic offset uncertainties as the square root of the sum of the pre- and post-earthquake site position uncertainties. Examples of coseismic offset determinations at campaign sites are shown in Supplementary Figure 1 (top). Coseismic offsets from campaign stations may

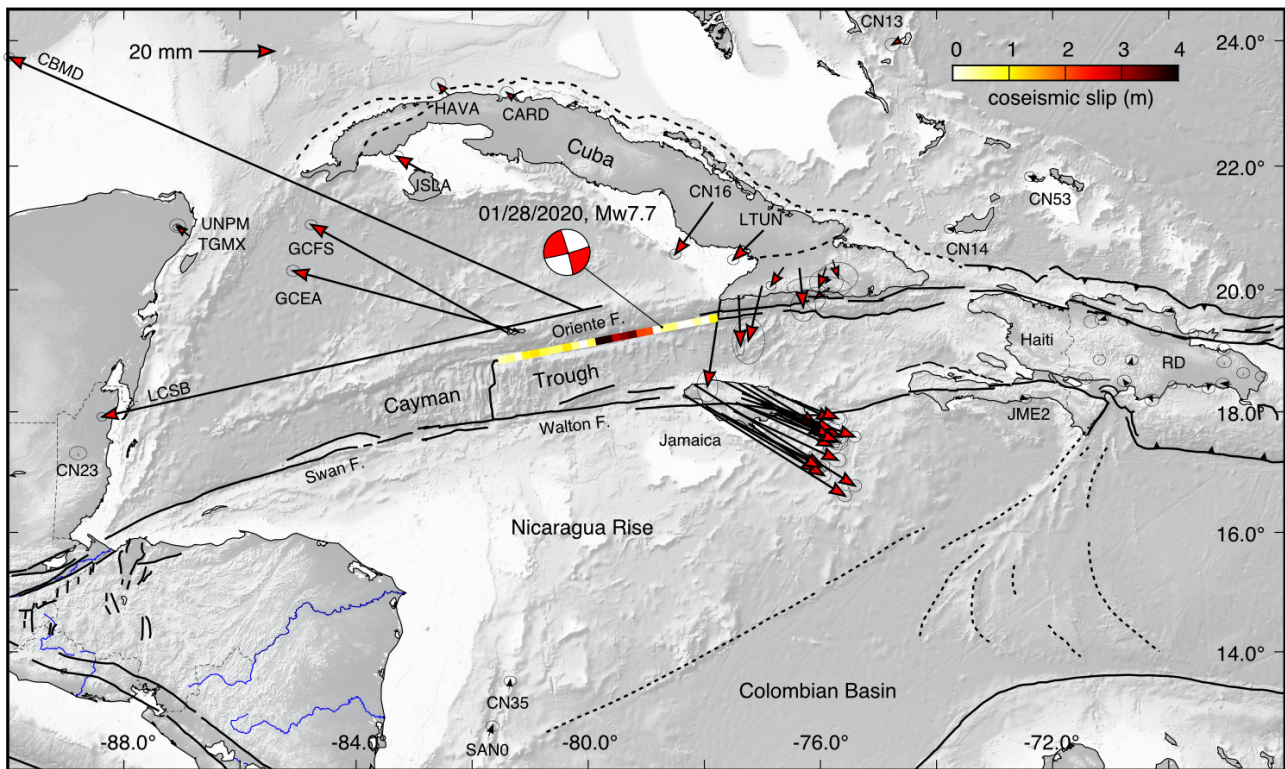


Figure 3 Map of horizontal coseismic offsets derived from GPS time series, as described in the text. The coseismic slip distribution estimated in the finite fault kinematic inversion is shown in color along the modeled rupture. Note the discernible coseismic offsets consistent with the rupture kinematics in the far-field of the rupture, including in the Bahamas (<4 mm), Yucatan (~4 mm), and Colombian Basin (2–3 mm).

be affected by postseismic deformation. However, comparisons of coseismic offsets between continuous and campaign sites that are nearly co-located show no significant difference.

Figure 3 shows the estimated horizontal coseismic offsets at GPS sites, and numerical values in the east, west and north directions are provided in Supplementary Table 1. They are consistent with expectations from a left-lateral strike-slip earthquake. In the near-field of the rupture, we observe horizontal offsets ranging from 6 to 17 cm on the Cayman Islands. Coseismic offsets are clearly visible in Cuba, all the way to Havana (site HAVA), with an offset of 4 mm. Discernible coseismic offsets are visible in the far field of the rupture, including in the Bahamas (<4 mm, sites CN14, CN53, CN13), Yucatan (~4 mm, sites UNPM, TGMX), and Colombian Basin (2–3 mm, sites SAN0, CN35). Coseismic offsets at campaign sites in Cuba and Jamaica are not as precisely determined as at continuous ones, but are generally consistent with nearby continuous sites. Offset uncertainties are particularly large in Cuba, as the campaign sites were observed at most twice in the 3 years preceding the earthquake. Coseismic offsets in Hispaniola (Haiti and the Dominican Republic) are not significantly different from zero, as the island lies within the alignment of the earthquake rupture strike.

3.2 Finite fault kinematic model

3.2.1 Seismic waveform data

Teleseismic data, henceforth referred to as TELE, consist of broadband P (vertical) and SH (horizontal transverse) displacement waveforms that we deconvolved from the instrument response, then bandpass filtered from 0.01 to 0.8 Hz for P-waves and 0.01 to 0.4 Hz for SH-waves. The analysis incorporates a total of 18 P-waves and 17 SH-waves collected from global stations situated at distances ranging from 30° to 90° relative to the mainshock epicenter (Supplementary Figure 2a). We compute synthetic waveforms using the method of Nabelek (1984). To accurately characterize the source area associated with the teleseismic waves, we use a one-dimensional velocity model that is a slight simplification of the CRUST2.0 model (Supplementary Table 2).

Regional broadband and strong motion records, hereafter referred to as RBBSM, contain the full waveforms from the P to the surface waves with their North-South (NS), East-West (EW), and vertical components. We selected 14 stations located at distances ranging between 140 and 1200 km from the rupture over a wide range of azimuths to the epicenter (Supplementary Figure 4b). The signal processing procedure involved amplitude correction via the sensitivity factor, elimination of the pre-event mean amplitude, double integration to obtain displacement, and bandpass filtering. We varied the low-frequency cutoff between 0.005 and 0.01 Hz based on the amount of long-period noise at each sta-

tion after double integration. Similarly, we varied the high-frequency cutoff between 0.03 and 0.08 Hz, contingent upon signal complexity and the feasibility of accurately modeling the waveforms using a simplified velocity structure. Synthetic seismograms were generated with the wavenumber integration method of [Bouchon \(1981\)](#), using the one-dimensional velocity model of [Moreno et al. \(2002\)](#) for the southern Cuban margin (Supplementary Tables 6 and 7).

We also used data from strong motion stations LCCY and FSCY located on the Cayman Islands, about 50 km from the earthquake rupture (Supplementary Figure 4b). However, we observed inconsistencies when these data were jointly inverted with those from the TELE and RBBSM stations. We analyzed and modeled the waveforms from these two stations for other earthquakes in the Caribbean and at teleseismic distances and found the same inconsistencies. Through comparative analysis with adjacent stations, examination of P-wave particle motion, and testing of various correction approaches, we determined that for both stations the North (N) and East (E) components had been inverted and that the amplitudes of the N, E, and vertical (Z) components were too large by a factor of about 2. An illustrative comparison with nearby broadband stations for a teleseismic event is presented in Supplementary Figure 2.

Our analysis indicates that both the broadband and strong motion records at LCCY and FSCY exhibit similar issues, as evidenced by their nearly perfect correlation between the integrated HN record (acceleration sensor) and the corresponding HH channel (velocity sensor) for the same component, following appropriate adjustments for instrument sensitivity. To further substantiate our findings, we conducted a comparison between the static displacement derived from the double integration of the horizontal strong motion records at station LCCY and the coseismic static offset recorded at the co-located GPS station LCSB. The results show good agreement, contingent upon exchanging the N and E components of LCCY and scaling them by a factor of two, as shown in Supplementary Figure 3.

Ultimately, we decided to incorporate stations LCCY and FSCY into the finite fault inversions after interchanging their N and E components and halving their amplitudes. We assigned these stations a weight reduced by a factor of ten relative to the other ones. Given that LCCY and FSCY are situated significantly closer to the rupture compared to the others, their amplitude – consequently their respective contribution to the root mean square (RMS) misfit function – remains substantial in the inversion process, notwithstanding the applied down-weighting factor.

3.2.2 Modeling procedure

We develop a kinematic slip model by inverting the GPS-derived static coseismic offsets and seismic waveforms described above, utilizing the nonlinear multiple windows method of [Delouis et al. \(2002\)](#). The spatial distribution of the GPS and seismic data is shown in Supplementary Figure 4. We model the rupture as a rect-

angular area 405 km in length and 32 km in width, with a strike of N78° and dipping 89° to the south. This geometric configuration is consistent with the moment tensor solutions documented for the earthquake (e.g., [USGS, 2020](#); [GEOSCOPE, 2021](#)). The rupture is partitioned into subfaults with a size of 15 km along-strike and 8 km along-dip. These subfaults serve as rectangular dislocation surfaces to calculate static surface displacements at the GPS stations, and their centers act as point sources for seismic waveform calculations. We refined the fault geometry parameters – azimuth, dip angle, dimensions, and fault location – through a series of inversions aimed at reaching an optimal fit to observational data. Furthermore, we allow for variations in rake of $\pm 50^\circ$ around the pure left-lateral strike-slip value of 0° .

The local source time function associated with each point source is represented by the sum of three overlapping isosceles triangular moment rate functions, each with a total duration of 8 s. The rupture onset times T_{onset} along the fault are limited by the bounding rupture velocities $V_{\text{rmin}} = 2.5$ km/s and $V_{\text{rmax}} = 5.5$ km/s, meant to enforce the constraints $V_{\text{rmin}} \leq D_{\text{sf}}/T_{\text{onset}} \leq V_{\text{rmax}}$, where D_{sf} is the distance from the subfault center to the earthquake hypocenter. The rupture onset time may vary freely within this defined range, so that the rupture speeds at any point of the fault, hereafter referred to as the local rupture speed, can lie beyond the $V_{\text{rmin}}-V_{\text{rmax}}$ range.

The inverted parameters for each subfault are the rupture onset time, the amplitudes of the three triangular source time functions, and the rake angle. The inversion utilizes a simulated annealing algorithm that seeks to minimize a cost function that is the weighted sum of the normalized RMS misfit functions for each dataset, plus a seismic moment minimization function and a smoothing function. We adjust the seismic moment minimization and smoothing functions weights to prevent incorporating excess seismic moment for minimal improvement in data fitting, and to avoid incorporating a level of model detail that is poorly resolved by the data. Given that teleseismic data typically exhibit lower resolving power compared to data recorded close to the source ([Delouis et al., 2002](#); [Bletery et al., 2014](#)), we assign the TELE dataset a weight of 0.5, in contrast to a weight of 1 for the RBBSM and GPS data.

Because of the earthquake's location offshore and the lack of proximal monitoring stations, the epicenter reported by seismological agencies is likely uncertain within a range of a few tens of kilometers. We therefore varied the hypocenter position – i.e., the rupture initiation location – to find the inversion that yielded the best fit to the data. We started with the epicenter coordinates provided by the USGS (19.419°N, -78.756°E) then tested alternative positions both to the east and west, while systematically exploring various depths. The optimal inversion result was achieved with an epicenter shifted approximately 30 km to the west of the USGS location at coordinates 19.349°N, -79.032°E, with a hypocentral depth of 12 km. The fit of the model results to the data, both the GPS coseismic offsets and the seismic waveforms, is in general very good to excellent, as shown in

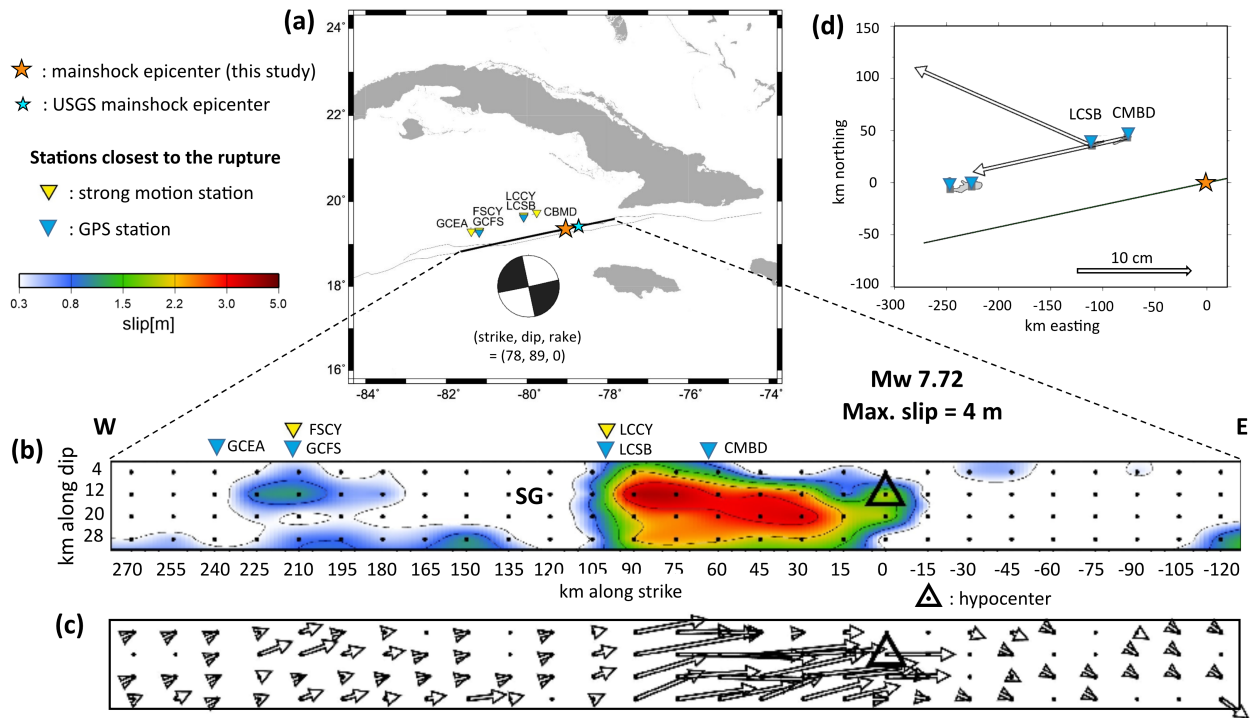


Figure 4 Slip distribution from the joint inversion of TELE, RBBSM and GPS data. (a) Map showing the surface trace of the fault model (heavy black line), the epicenters from this study and from the USGS, and the focal mechanism corresponding to the fault model. (b) Slip distribution along the fault model. The projection onto the fault trace of the closest strong motion and GPS stations are shown on the top. Small black dots are the grid of point sources along the fault model. SG: slip gap. (c) Slip vectors, size proportional to slip and same dimensions as shown in (b). Arrows show the static coseismic displacement of the southern block with respect to the northern one. (d) Observed coseismic displacement at stations CMBD and LCSB, displaying a 40° change in direction.

figures 6 and 7.

3.2.3 Final slip distribution and rupture timing

The final slip distribution from the joint inversion of TELE, RBBSM, and GPS static data (Figure 4) shows a rupture that is largely unidirectional toward the west. From the hypocenter, a substantial area of slip is observed extending approximately 100–110 km westward and 0–20 km in depth, with a maximum slip of approximately 4 m. The western limit of this slip region is well-constrained in the model due to static coseismic displacements from continuous GPS stations CMBD and LCSB, located about 40 km apart on Grand Cayman island (Figure 4d). Coseismic displacement rapidly changes direction from rupture-parallel at site CMBD to striking 40° relative to it at site LCSB. This rapid change in the direction of surface coseismic displacement is consistent with an abrupt termination of slip on a left-lateral strike-slip rupture, which has to occur in the vicinity of station LCSB.

Immediately to the west of the primary slip zone, the rupture vanishes abruptly, delineating a slip gap (denoted SG in Figure 4b) within the depth range of 0–20 km. Below this range, in the deeper section of the fault, the model assigns a patch of moderate slip. Further westward, at distances between 180 and 230 km from the hypocenter, the model identifies a secondary

slip region also within the 0–20 km depth range, where slip reaches up to 1.1 m. In contrast, slip is minimal east of the hypocenter. The small patch observed in the lower eastern corner of the model should not be considered reliable, as the fault system becomes geometrically more complex east of the epicenter, with multiple branches, as one approaches the Cabo Cruz pull-apart basin. Since we model the rupture with a single fault plane, it is possible that this small slip patch is a biased attempt of the inversion to account for slip occurring on a secondary fault branch. The model rake is close to pure left-lateral strike-slip along most of the rupture, consistent with moment tensor solutions.

The onset of slip as a function of distance to the epicenter derived from the final slip distribution inversion, displayed in Figure 5, shows a local rupture speed of 3–3.5 km/s for the first ~20 s or ~60 km. Rupture then accelerates to close to 4 km/s for 10 s/40 km in the area delineated as FLVR1 in Figure 5. Since shear wave velocity in the crust here ranges from 2.82 to 3.97 km/s (Supplementary Table 2), the rupture was then propagating at supershear speed. This is consistent with the back-projection results, which will be described in more detail below, although the kinematic inversion places the rupture front slightly ahead of that of the back-projection. Further to the west, in the slip gap, timing information is only provided by the back-projection, which does identify supershear rupture speed. In the

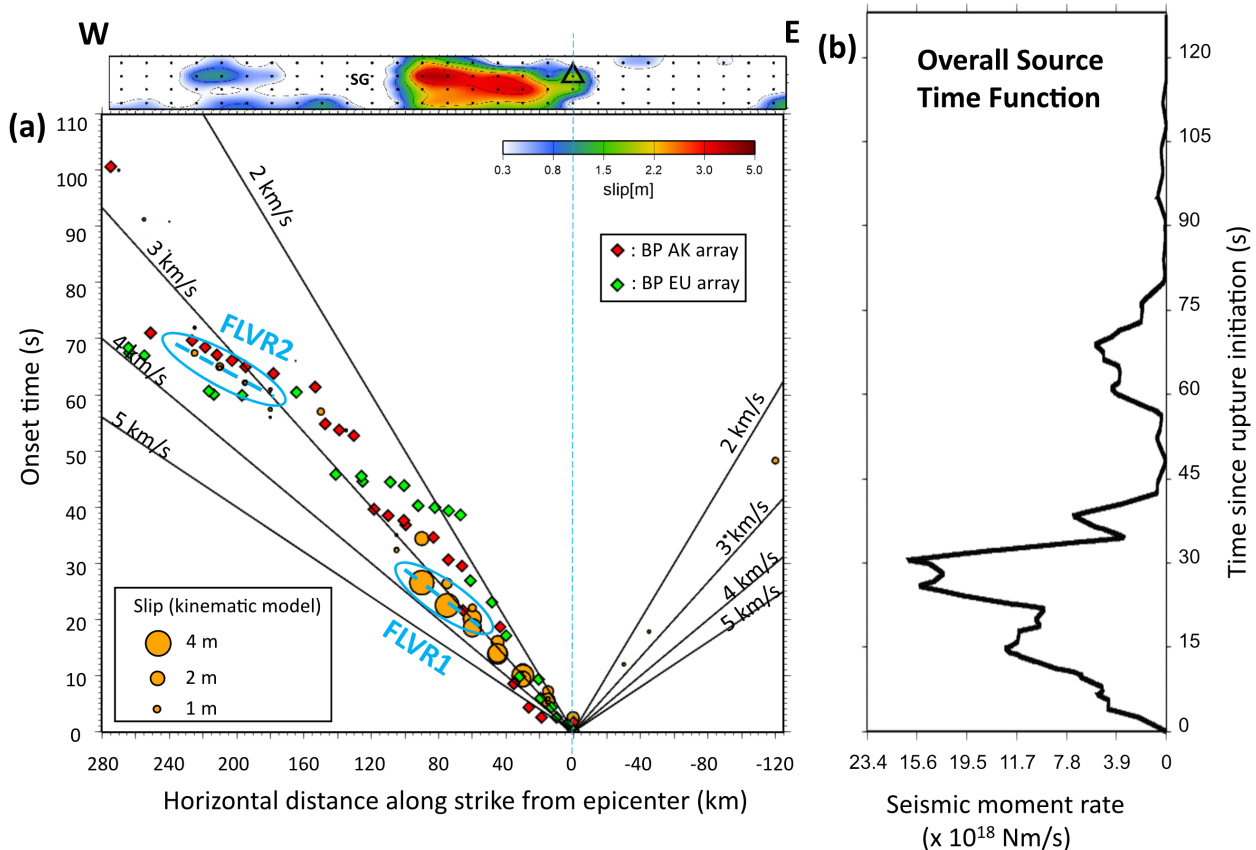


Figure 5 (a) Time-distance plots of coseismic slip on the model fault plane. Orange circles: subfault onset time – *i.e.*, time when the subfault is triggered and begins to slip – as a function of distance to the epicenter, with size proportional to slip. Oblique black line show average rupture speeds of 2, 3, 4, and 5 km/s, for visual reference. The blue dashed lines and contoured areas marked FLVR1 and FLVR2 indicate fault segments where the local rupture velocity shows particularly high values, close to or above 4 km/s. Here shear wave in the crust is between 2.82 and 3.97 km/s (see Supplementary Tables). Diamonds show rupture timing from the back-projection method, red for the Alaska seismic array (AK), green for the Europe seismic array (EU). The slip distribution along fault strike and dip from Figure 4 is shown above the graph, with the slip gap described on the text marked SG. (b) Rupture source time function from the final finite fault model.

westernmost portion of the rupture, the kinematic inversion and the back-projection coincide and identify a local rupture velocity close to 5 km/s, clearly supershear, in the area labeled FLVR2 in Figure 5a.

The source time function (Figure 5b) shows a prominent initial release of seismic moment between 0 and 30 s, which coincides with the primary slip region depicted in Figure 4. This initial burst is followed from 35 to 55 s by a gap in seismic moment release, then a secondary surge of moment release from 55 to 80 s, which corresponds to the previously mentioned supershear segment FLVR2 (Figure 5a).

To test the sensitivity of the results to stations FSCY and LCCY, we performed two additional inversions, one with a weight of zero for those stations and the other with an intermediate weight of 0.05. The results, presented in Supplementary Figures 7 and 8, and in Supplementary Table 8, are stable in terms of slip distribution and rupture timing. As one should expect, the waveform fit at those stations worsens as the weight decreases, particularly for a weight of zero. We observe a slight dependence of the maximum slip and average rupture velocity, which, respectively, increase and de-

crease as the weight is decreased. In any case, the main conclusions of this work remain valid when the FSCY and LCCY stations are omitted or their weight is varied in the inversion.

3.2.4 Resolution test

To test the spatial and temporal resolution of the kinematic inversion described above, we designed the synthetic model with variable slip and rupture velocity illustrated in Supplementary Figure 5a-b-e. We used this model to generate synthetic displacement waveforms and static offsets at the TELE, RBBSM and GNSS stations used in the inversion of the real data. We randomly altered the amplitudes of the synthetic data by factors of 1.1 or 0.9, corresponding to a 10% modification at each station. We also used a slightly modified one-dimensional velocity model to compute the Green's function to avoid unrealistically ideal conditions. The velocity model applied in the inversion is given in Supplementary Tables 2 and 3, and the one used to generate the synthetic data is presented in Supplementary Tables 4 and 5. We then inverted the modified synthetic data

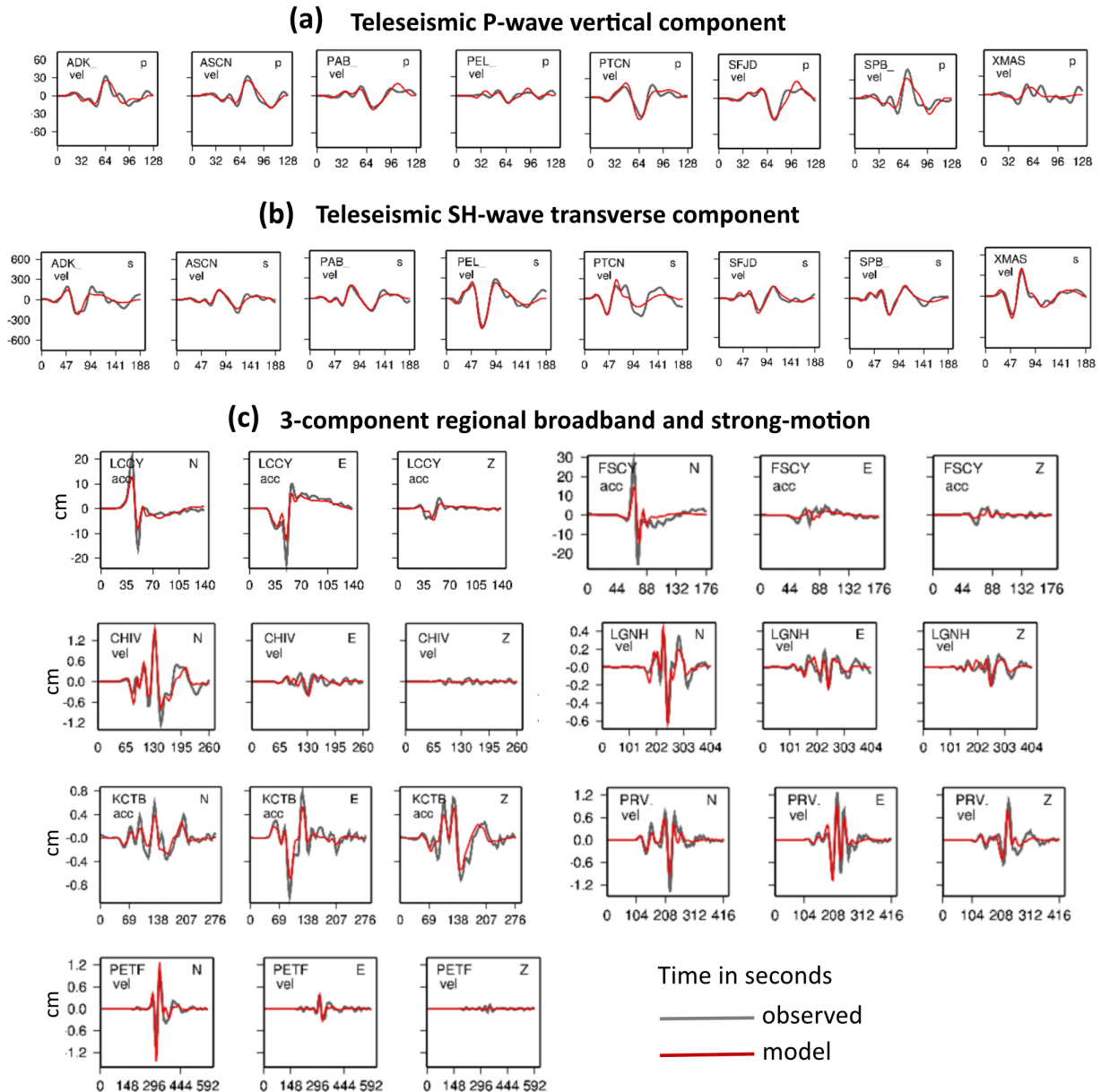


Figure 6 Waveform fitting of a selection of stations using the model obtained by the joint inversion of TELE, RBBSM and GPS data. (a) and (b) show teleseismic (TELE) displacement waveform fitting, for the P and SH-waves respectively. vel: broadband velocity sensor. (c) Regional broadband and strong motion (RBBSM) waveform fitting. N, E, Z: north, east, vertical (up) components respectively. All displacement waveforms are bandpass filtered. acc: strong motion sensor; vel: broadband velocity sensor.

using exactly the same rupture parameterization and algorithm as for the real data inversion.

This inversion of synthetic data, as illustrated in Supplementary Figure 5c-d-f, successfully identifies the primary slip zones a1 to a4 of the synthetic model, although with some degree of smearing and spreading compared to the input model. Synthetic slip area a2, located within the slip gap of the real data inversion (designated SG in Figure 4b), is retrieved despite its alignment with a gap between adjacent strong motion and GPS stations (Figure 4b). This suggests that the slip gap identified from the real data inversion does not stem from an absence of proximal stations but rather represents a true characteristic of the kinematic inversion. We also note a con-

sistent trend of the synthetic inversion to retrieve slip at slightly greater depths than those in the input model. This may be due to the chosen velocity model and/or the lack of monitoring stations directly above the rupture. The input rake is well recovered along the entire rupture area.

Rupture timing is also generally recovered, also with some spread compared to the input model (Supplementary Figure 5e-f). The input local velocity along slip area a1 is recovered with a subshear velocity of 3 km/s for the initial 20 s/60 km, accelerating to close to 4 km/s for the next 10 s/40 km. The synthetic local rupture velocity of 3 km/s along slip area a2 is recovered, though with significant smearing. Supershear rupture speed along area

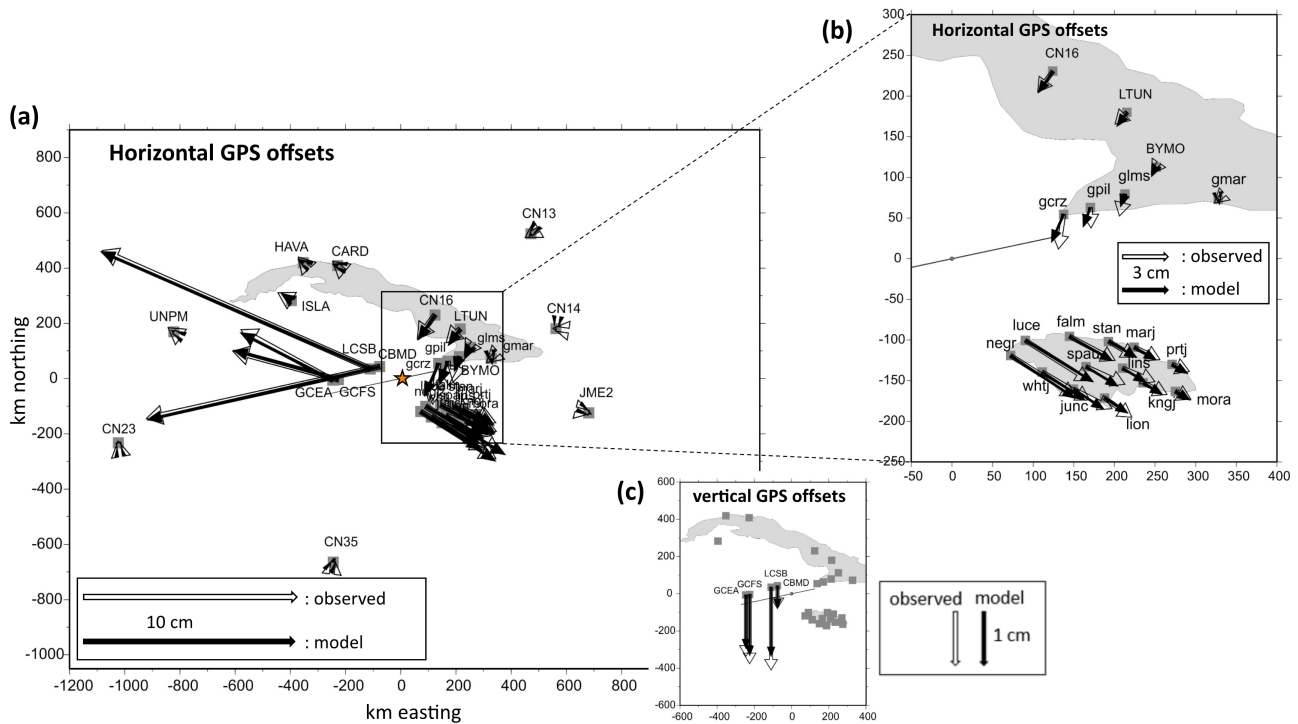


Figure 7 Coseismic offset fitting at the GPS stations used in the joint inversion of TELE, RBBSM and GPS data. (a) and (b) show horizontal offsets, and (c) shows vertical offsets at the continuous stations on the Cayman Islands. The model fit is within observational uncertainties at all stations, including for the vertical component at the Cayman Islands stations.

a3 is generally recovered.

To assess whether the near 4 km/s rupture velocity along the FLVR1 segment may be overestimated by the inversion procedure, we conducted an additional synthetic test using an input model in which the rupture velocity is subshear along that segment. The result is presented in Supplementary Figure 6, in which panels (e) and (f) show that the inverted rupture times along the aforementioned segment remain close to, or even slightly lower than, the average 3 km/s reference line. However, points within that particular segment tend to align in a way that suggests a rupture speed that locally exceeds 3 km/s, *i.e.*, larger than the input synthetic value. This means that the local slope of about 4 km/s along the FLVR1 segment in the real data inversion should be considered with caution. We conclude that the rupture speed along the FLVR1 segment is within the range of 3.5 to 4 km/s, possibly supershear but with some uncertainty.

3.3 Back-projection

To further evaluate the kinematic rupture process and assess its potential supershear characteristics, we employed teleseismic P-wave back-projection, henceforth referred to as BP. The development of dense regional seismic arrays has rendered BP an invaluable technique for delineating the rupture length, direction, speed, and segmentation of large earthquakes. The BP technique, independent of prior knowledge of fault geometry or rupture speed, identifies the location, timing, and relative energy of high-frequency sources by tak-

ing advantage of the coherence of seismic waveforms across dense observational networks. In this study, we use the Slowness-Enhanced Back-Projection (SEBP) method (Meng et al., 2016; Bao et al., 2019), which integrates aftershock-based calibration to address slowness bias and mitigate three-dimensional path effects. SEBP reduces mislocation artifacts arising from heterogeneous velocity structures, thereby enhancing the precision of rupture speed estimations through calibration of wave path effects using adjacent events with magnitudes ranging from 4 to 6 (Bao et al., 2019).

We applied the SEBP method to P-wave seismograms obtained from 211 broadband stations from the Alaska network (AK) and 301 stations from the European network (EU) (Supplementary Figure 9). A first version of this analysis was presented by Bao et al. (2022). The P-waves were filtered within a frequency range of 0.5 to 2.0 Hz for the AK array, and 0.4 to 1.0 Hz for the EU array, selecting the highest frequency range that permitted sufficient waveform coherence. This coherence is defined by mutual correlation coefficients greater than 0.85 during the initial 10 s of the P-wave. The frequency range for the EU array is slightly lower due to its larger azimuthal and distance coverage (Supplementary Figure 9), which leads to lower coherence at higher frequencies. To align waveforms, we utilized a 6-s window centered on the P-arrival, employing multi-channel cross-correlation. Subsequently, we back-projected the waveform utilizing a sliding window of 10 s with increments of 1 s. Because of its limited depth sensitivity, the BP is performed at the fixed depth of 14.9 km.

We calculated the slowness correction terms using

data from seven nearby earthquakes that are evenly distributed on either side of the mainshock rupture, with magnitudes ranging from 4.5 to 6.1. Since an accurate location of these events is important for reliable slowness calibrations, we used the double-difference relocation results described in section 3.4, whose relative uncertainty is 2–5 km, significantly smaller than the 26–28 km RMS errors of BP locations.

The implementation of slowness calibration results in (1) a substantial decrease in spatial bias, with a reduction of RMS errors from 26.4 km to 11.8 km for the AK array and from 28.8 km to 16.9 km for the EU array, and (2) an improved alignment of BP source locations with the Oriente fault trace.

Figure 8 shows the spatial and temporal distribution of high-frequency sources obtained from the SEBP method after removal of the BP artifacts. These artifacts are apparent high-frequency radiations off the main rupture, with apparent rupture stagnation and back-propagating fronts, which are due to abrupt changes in rupture speed – in particular at the sub- to super-shear transition – and in slip distribution along the rupture. As a result, Figure 8 only shows the so-called “leading radiators” of the earthquake rupture as imaged by the SEBP method. We observe a high degree of consistency between results from the AK and EU seismic networks, with high-frequency leading radiators that align well with the key characteristics identified in the finite fault inversion.

Spatially, the high-frequency sources exhibit a predominantly linear rupture trajectory that extends toward the WSW. They are superimposed onto the Oriente fault trace within the uncertainty of the source localization by the BP method (Figure 8, top). Time-wise, the BP model delineates two distinct episodes of rupture: an initial phase characterized by subshear speed propagation at about 3 km/s for a duration of 20–30 s and along 40 to 50 km, followed by an acceleration to supershear velocity at a speed greater than 4 km/s, lasting about 40 s over a distance of about 200 km (Figure 8, bottom). The transition from subshear to supershear as derived from the BP method is therefore consistent with the results from the finite fault inversion described above (see Figs. 5 and 8).

3.4 Aftershock analysis

Supershear earthquakes are characterized by a rupture with fewer aftershocks and a smaller moment release than subshear ones, while aftershocks tend to concentrate on secondary faults off the main rupture (Bouchon and Karabulut, 2008). We used data from the Cuban, Cayman Islands, and Jamaican seismic networks, together with additional regional seismic stations, to relocate aftershocks using the double-difference method of Waldhauser (2001). The method takes advantage of the fact that, if the hypocentral separation between two earthquakes is small compared to the event-station distance and the scale length of velocity heterogeneity, the ray paths between the source region and a common station are similar, so that the difference in travel time for two earthquakes observed at one station can be at-

tributed to the spatial offset between the events with high precision. Event pairs are selected on the basis of their hypocenter distance and waveform similarity, measured through a cross-correlation function. Here, we used an event-pair distance of 10 km and a minimum correlation coefficient of 0.7.

We relocated a total of 707 events spanning January 28 to December 31, 2020, using the velocity model described in Moreno et al. (2002). Their temporal distribution qualitatively follows Omori's law (Figure 9 bottom left), while their frequency-magnitude distribution, with a magnitude of completeness on the order of 2.5, shows a significant deficit in larger magnitude events (Figure 9 bottom right). Here, magnitudes are local. Indeed, only 8 aftershocks of a magnitude greater than 4.5 have been recorded; three of these have a magnitude greater than 5, and the largest one has a magnitude of 6.0 (Figure 10). This is well below the value expected from Båth's law, which states that the magnitude difference between the mainshock and the largest aftershock is on average 1.2.

We estimated the b -value of the Gutenberg-Richter law $\log_{10} N(\geq m) = a - bm$ for the frequency-magnitude distribution of aftershocks using both the maximum likelihood method of Aki (1965) and Utsu (1965), and a linear fit to the binned distribution. Here, $N(\geq m)$ is the number of earthquakes with magnitudes greater than or equal to m , while a and b are constants. We performed the calculation while varying the minimum magnitude above which the aftershock catalog is complete as well as the distribution bin width. In all cases, we find a b -value close to 0.7, significantly lower than the typical b -value of ~ 1 found for many earthquake catalogs, and at the low end of the $0.3 \leq b \leq 2.5$ range reported by El-Isa and Eaton (2014). Variations in b -value are classically attributed to variations in stress, with b -values decreasing as differential stress increases (Scholz, 1968; Schorlemmer et al., 2005; Scholz, 2015). The b -value found here is therefore consistent with a fault zone at high stress, hence promoting rupture at supershear speed.

In map view, the aftershock distribution matches the location and length of the Oriente fault segment that ruptured in the mainshock well (Figure 10, top). However, $\sim 75\%$ of the aftershocks are located in the westernmost part of the rupture, surrounding the three $M \geq 5.0$ events of the sequence (Figure 10, middle). In contrast, the central part of the rupture, where coseismic slip was greatest and the rupture transitioned to supershear velocity, is relatively devoid of aftershocks, with no event greater than magnitude 4.5. This pattern is consistent with other observations of aftershock sequences following supershear earthquakes, with a rupture plane that is seismically quiet whereas aftershocks cluster off the fault – here in the westernmost part of the rupture – on secondary structures, and where a scarcity of aftershocks has been interpreted as secondary faults being triggered during the mainshock (not after it) by the high dynamic stresses that accompany the supershear rupture (Bouchon and Karabulut, 2008; Jara et al., 2021).

Thus, the distribution of aftershocks following the 2020 Cayman Through earthquake bears similarities

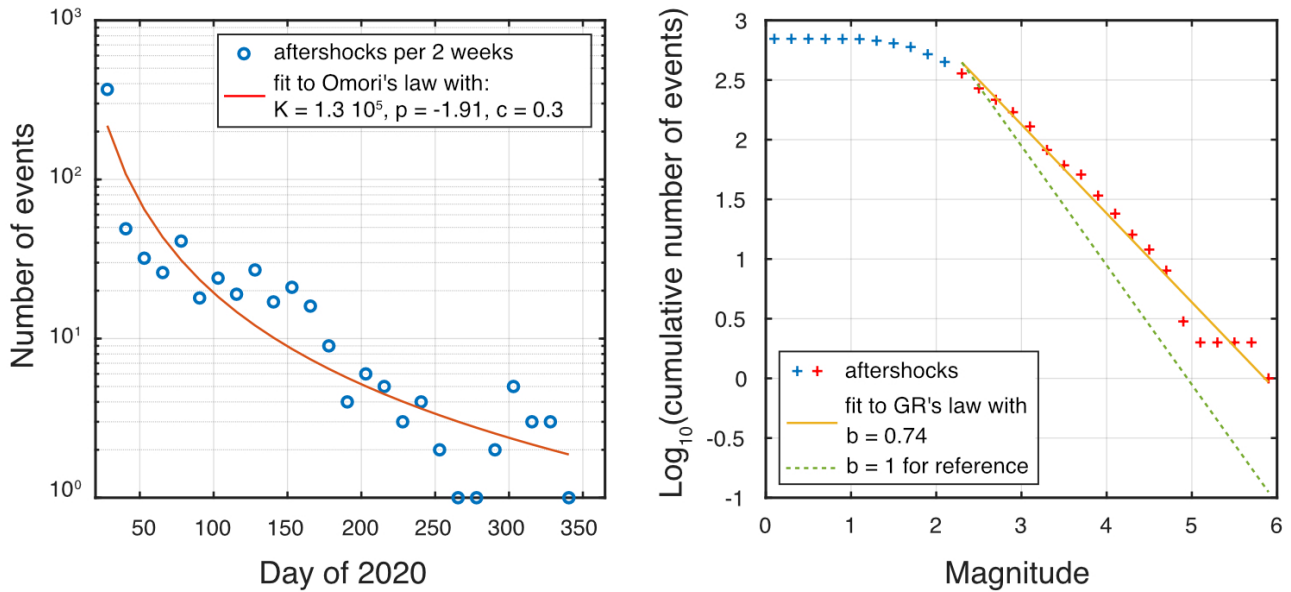
707 events, 312 $M > M_c$ 

Figure 9 Left: distribution of aftershocks as a function of time. Aftershocks are binned in 2 week time intervals. The red line shows a fit to Omori's law, $n(t) = K(t + c)^{-p}$, where n is the number of events as a function of time t , and K, c, p are empirical parameters. Right: cumulative distribution of aftershocks as a function of magnitude. The orange line shows the fit to a Gutenberg-Richter law (explanations in the text) for aftershocks above the magnitude of completeness, shown with red crosses.

with other supershear ruptures, with a post-mainshock quiescence of the fault, the activation of off-fault structures, and a paucity of large magnitude events resulting in an overall moment release lower than expected given the mainshock magnitude. These observations have been interpreted as the result of relatively uniform friction along supershear segments, together with the high dynamic stresses carried by the shock wave radiation at large distances from the main fault (Bouchon and Karabulut, 2008).

4 Discussion

The observations and model results described above confirm the supershear nature of the 28 January 2020, $M_w 7.7$, Cayman Trough earthquake, as proposed by Tadapansawut et al. (2020) on the basis of teleseismic P-waveforms and Bao et al. (2022) on the basis of back-projection imaging. The extensive data set used here, which includes local, regional and global seismic waveforms, local and regional coseismic geodetic offsets, and relocated aftershocks, provides a comprehensive and detailed description of the rupture. Taken together, our data and models are consistent with a rupture that propagated predominantly unilaterally westward, with an initial phase at subshear speed for 20–30 s and over 40 to 50 km, followed by an acceleration to supershear speed, which persisted all the way to the western end of the rupture, for 40 s and over about 200 km. There is unfortunately no strong motion recording to test the criterion often invoked for supershear rupture that the fault-parallel to fault-normal ground velocity ratio is greater than 1 at close distance to the rupture (Ellsworth

et al., 2004; Dunham and Archuleta, 2004; Amlani et al., 2022). Theoretical models indicate that this property is valid within at most 10 km of the rupture (Aagaard and Heaton, 2004; Mello et al., 2014), while strong motion stations FSCY and LCCY here are located about 50 km from it (Supplementary Figure 9b).

Our results show two main differences with those of Tadapansawut et al. (2020). First, we do not observe supershear rupture speed initially, but a transition from subshear to supershear after 20–30 s, which is marked by a burst of high-frequency radiation in the BP data. Second, BP imaging and kinematic inversion both show supershear speed for the rest of the rupture. Also, we find that the geometry of the supershear segment does not show much complexity, as it follows a linear segment of the Oriente fault, well-marked in the bathymetry as a series of *en échelon* ridges cutting through a narrow, elongated basin at the toe of – and parallel to – the Cayman Ridge (Figure 2). This is consistent with many observations of large strike-slip earthquakes, where supershear rupture is systematically associated with segments that have a simple, linear geometry, with small or absent segmentation features (Bouchon et al., 2010). Laboratory experiments also show that supershear ruptures favor propagation along straight faults – if they are available – rather than branching onto more complex fault segments (Rousseau and Rosakis, 2009; Templeton et al., 2009). Interestingly, the supershear rupture stopped in an area where the Oriente fault geometry becomes more complex than a single linear segment, as it emerges from the narrow basin mentioned above and splits into two sub-parallel segments on either side of an elongated ridge

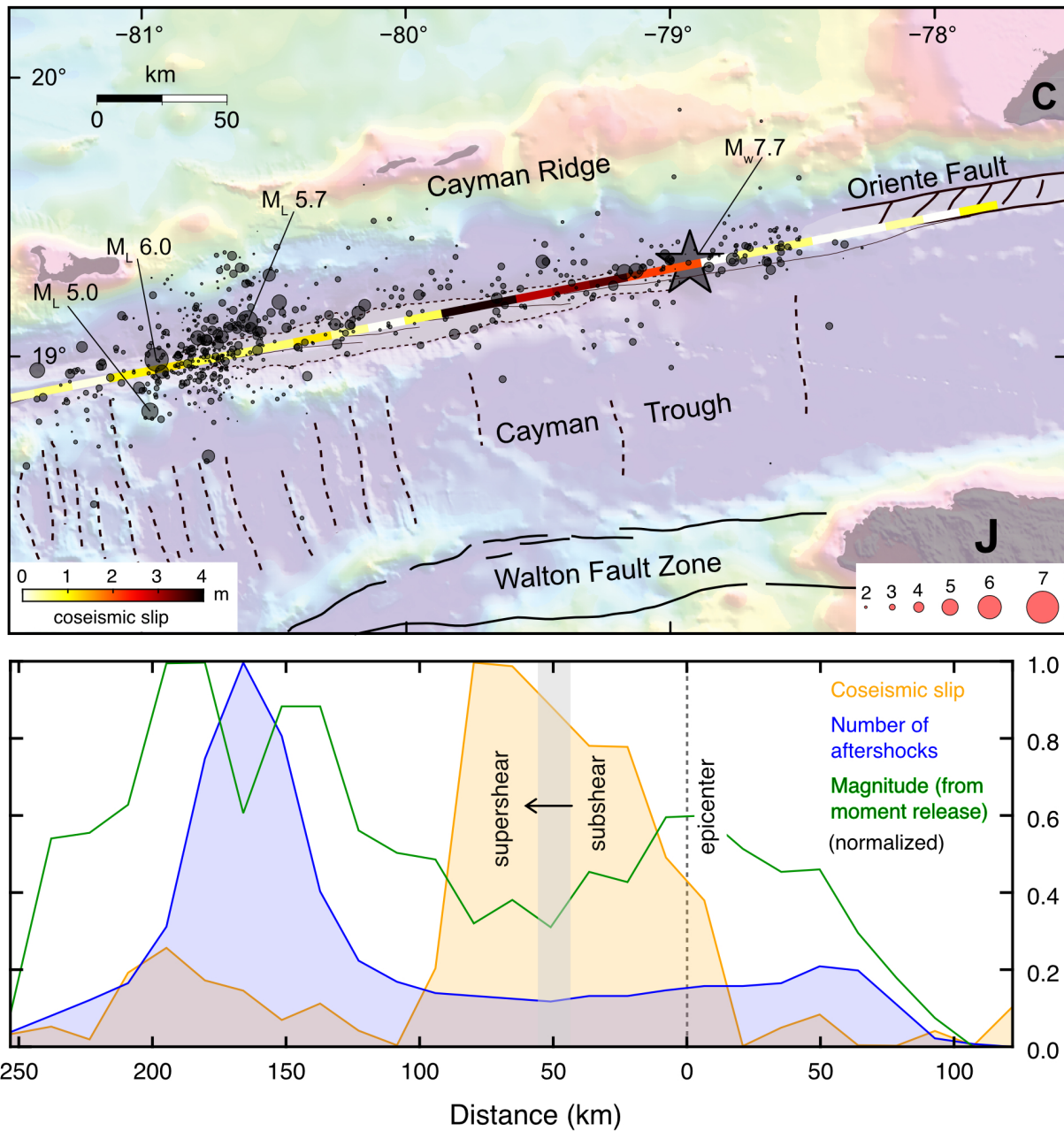


Figure 10 Top: relocated aftershocks from January 28th to December 31th, 2020, shown with gray circles sized as a function of their magnitude, on top of the bathymetry (colored background) and main active faults (black lines). The gray star shows the mainshock epicenter location. Coseismic slip from the finite fault kinematic model is shown as a thick line in white/yellow/red/black color. The three aftershocks with a local magnitude greater than 5, located near the western end of the rupture, are indicated. Bottom: distribution of coseismic slip (orange), number of aftershocks (blue, bins of 15 km), and aftershock seismic moment release (green dashed line) as a function of distance along the earthquake rupture. Values are normalized and the distance axis in km coincides with the rupture length on the top subplot.

(Figure 2).

Although the rupture maintains supershear speed once it transitions, the finite-fault model clearly shows a slip gap (SG) separating two supershear patches (Figure 4). One interpretation consistent with this slip gap is the mechanism known as “barrier-induced supershear” found in numerical simulations (Dunham, 2007; Lapusta and Liu, 2009; Weng et al., 2015). In this mechanism, a rupture arrests on a barrier and transfers stresses to the fault segment beyond the barrier; the resulting higher stresses there favor re-nucleation and supershear rupture. Alternatively, noting that the finite

source inversion model shows low-amplitude slip below the slip gap, it is possible that the back-projection images a deep, continuous part of the rupture that radiates sufficiently at high frequencies despite its small (low-frequency) slip. In fact, high- and low-frequency slip have been observed to occupy different areas of the rupture in the 2011 Tohoku earthquake (Meng et al., 2011) and other large events (Lay et al., 2012).

In the model proposed by Weng and Ampuero (2020), supershear ruptures are favored on faults that have been able to accumulate high stresses without generating a large earthquake in the recent past. Such earlier

ruptures, at lower stresses, would have been subshear. This model feature would be supported by a low level, or even lack, of prior seismicity on the future supershear fault segment, as a low seismicity rate, implying a low rate of earthquake nucleations, enables the build-up of tectonic stress above the stress level required for a large subshear earthquake. This low level of seismicity is indeed observed in the earthquake catalog prior to the Cayman Trough earthquake, as shown on Figure 1B: the Oriente fault segment that ruptured at supershear speed on 28 January 2020 had not experienced significant seismic activity ($M > 6$) for at least one century.

From the theoretical model of Weng and Ampuero (2020), we derive that the quiescence necessary to enable supershear rupture is only a small fraction of the recurrence time of subshear earthquakes. Elastic energy is proportional to the square of the excess stress above dynamic friction strength, which controls the potential stress drop. If stress accumulates linearly with time, elastic energy therefore accumulates quadratically. In this model (see Figure 3 in Weng and Ampuero (2020)), the minimal energy for large supershear earthquakes is larger than that for subshear earthquakes by a factor of about 1.45. Thus, for a supershear rupture to occur, quiescence must delay earthquake nucleation by at least a factor of $\sqrt{1.45} \sim 1.2$, that is 20%, relative to the minimum recurrence time of subshear events. This number is smaller than typical values of the coefficient of variation of earthquake recurrence times on strike-slip faults. Thus, it is reasonable to expect that earthquakes that were relatively “overdue”, *i.e.*, towards the higher end of the fault’s recurrence time distribution, could reach supershear speeds.

Supershear ruptures also have a specific behavior when they propagate along fault interfaces with material contrasts (Andrews and Ben-Zion, 1997). Rupture along such a bimaterial interface indeed breaks the stress symmetry and produces a coupling effect between the local normal stress and the interface slip. As a result, normal stress and frictional strength are dynamically reduced when a supershear rupture propagates in the direction of motion of the more compliant side of the fault, usually referred to as the “negative direction” (Weertman, 2002). This makes the negative direction favored for supershear ruptures, while the sub-Rayleigh propagation favors the opposite, “positive direction”. Supershear rupture in the positive direction is possible, yet rare in both numerical (Shi and Ben-Zion, 2006) and experimental studies (Shlomai and Fineberg, 2016; Shlomai et al., 2020). It has been proposed that the 1997 Izmit earthquake ruptured along the positive direction at supershear speed (Bouchon et al., 2001), though this observation has been debated (Weertman, 2002; Bouchon and Rosakis, 2002). The Cayman Trough earthquake rupture separates the stiffer, more compliant oceanic lithosphere of the Cayman Trough from the softer island arc material of the Cayman Ridge. This, with the left-lateral nature of the event, makes westward propagation the positive direction. Considering the comprehensive documentation of westward propagation at supershear speed, the Cayman Trough earthquake provides observational evidence that supershear

ruptures can propagate in the positive direction.

Finally, the 28 January 2020, $M_w 7.7$ earthquake rupture coincides with a segment of the Oriente fault where the locking depth derived from GNSS measurements of interseismic strain rates is less than 5 km, hence significantly reduced compared to the 15–25 km global average for strike-slip faults in a similar thermal regime (Verdant, 2015) or to the adjacent, eastern Cuba segment with a 25 km locking depth. Theoretical considerations from fracture mechanics theory for long ruptures show that supershear rupture is favored by a low G_c/G_o ratio, where G_c is the fracture energy dissipated near the rupture front and G_o the static elastic energy release rate (Weng and Ampuero, 2020). Supershear rupture is therefore favored by a large G_o . Following equation 20 of Weng and Ampuero (2020), $G_o = C \mu D^2/W$, where C is a geometric factor of order 1, μ is the shear modulus, D is the coseismic slip, and W is the rupture depth (or width). For a given interseismic slip deficit D , fault segments with smaller W , hence shallower locking depth, have a larger G_o and are therefore more likely to host supershear ruptures. Both quiescence and shallow locking are observed in the rupture area, but not in the unbroken fault segment east of the mainshock. This speculatively suggests that large earthquakes on that eastern segment would be less likely to go supershear. However, we cannot determine which of the two factors, quiescence or shallow locking, might be the dominant one in the supershear rupture documented here.

5 Conclusion

The 28 January 2020, $M_w 7.7$ Cayman Trough earthquake is the largest magnitude event of the instrumental seismology era to strike the northern Caribbean transform plate boundary. Observational evidence and models indicate that the event, supershear over most of its length, ruptured a linear, unsegmented portion of the Oriente fault where earthquake nucleation is infrequent and interseismic locking depth is shallow. These two characteristics translate into (1) the accumulation of a large amount of elastic energy over a long fault segment during the interseismic time interval, and (2) a fundamental propensity for this segment to host supershear ruptures (Weng and Ampuero, 2020). This provides a possible explanation for the unusually large magnitude supershear earthquake of 28 January 2020 along the Oriente transform fault.

Acknowledgements

We acknowledge funding from the FEDER European Community program through the Interreg Caraïbes “PREST” project, grant number 5236, and from the French National Research Agency, “CAST” project, grant number ANR-22-CE01-0019. We acknowledge the support of the Joint International Laboratory “Caribact”. JPA was supported by the French government through the UCAJEDI Investments in the Future project (ANR-15-IDEX-01) managed by the National Research Agency (ANR). The Jamaica GPS site occupations were funded by the NSF RAPID Award EAR-2022468 to

C. DeMets. We thank the French mobile GNSS instrument pool GPSmob of Resif-Epos, managed by CNRS-INSU, for lending instruments for campaign measurements in Cuba. Many thanks to Neal Lord of the University of Wisconsin for completing his GPS field work in Jamaica even as COVID-19 spread through the island. The authors thank the International GNSS Service (IGS) and its data and analysis centers, as well as UNAVCO, for providing open-access GNSS data and data products to the community. The authors thank Lee Madison from the Cayman Island Department of Public Safety Communications for sharing information on strong motion data. We thank the anonymous reviewers for their insightful comments and suggestions.

Data and code availability

Broadband and strong motion seismic records were retrieved from the IRIS data center (<https://ds.iris.edu/ds/nodes/dmc/>, last accessed on June 6, 2023). Data from continuous GPS stations in Cuba are proprietary and were provided by GEOCUBA. Most of the other continuous GPS stations used here are part of the COCONet project, now incorporated into the Network of the Americas, operated by UNAVCO, and supported by NSF under awards EAR-104296 (UNAVCO) and EAR1042909 (UCAR). GPS data were retrieved from the UNAVCO data center at <http://data-out.unavco.org>, and the IGS data centers at <http://garner.ucsd.edu> and <http://cddis.nasa.gov>. Some of the figures were made with the Generic Mapping Tools (GMT, (<https://www.generic-mapping-tools.org/>, Wessel et al., 2019). The CRUST2 model was retrieved from <https://igppweb.ucsd.edu/~gabi/crust2.html> (last accessed on June 6, 2023). Seismic data processing was performed in part using the Seismic Analysis Code (SAC) package by Goldstein et al. (2003) and Goldstein and Snoke (2005, <http://ds.iris.edu/ds/nodes/dmc/software/downloads/sac/102-0/> (last accessed on June 6, 2023).

Competing interests

The authors declare that they have no known competing financial interests or personal relationships that could have appeared to influence the work reported in this publication.

References

- Aagaard, B. T. and Heaton, T. H. Near-Source Ground Motions from Simulations of Sustained Intersonic and Supersonic Fault Ruptures. *Bulletin of the Seismological Society of America*, 94(6): 2064–2078, 2004. doi: 10.1785/0120030249.
- Aki, K. Maximum likelihood estimate of b in the formula $\log N = a - bM$ and its confidence limits. *Bulletin of the Earthquake Research Institute*, 43:237–239, 1965.
- Amlani, F., Bhat, H. S., Simons, W. J. F., Schubnel, A., Vigny, C., Rosakis, A. J., Efendi, J., Elbanna, A. E., Dubernet, P., and Abidin, H. Z. Supershear shock front contribution to the tsunami from the 2018 Mw 7.5 Palu, Indonesia earthquake. *Geophysical Journal International*, 230(3):2089–2097, 2022. doi: 10.1093/gji/ggac162.
- Andrews, D. J. and Ben-Zion, Y. Wrinkle-like slip pulse on a fault between different materials. *Journal of Geophysical Research: Solid Earth*, 102(B1):553–571, 1997. doi: 10.1029/96jb02856.
- Bao, H., Ampuero, J.-P., Meng, L., Fielding, E. J., Liang, C., Milliner, C. W. D., Feng, T., and Huang, H. Early and persistent supershear rupture of the 2018 magnitude 7.5 Palu earthquake. *Nature Geoscience*, 12(3):200–205, 02 2019. doi: 10.1038/s41561-018-0297-z.
- Bao, H., Xu, L., Meng, L., Ampuero, J.-P., Gao, L., and Zhang, H. Global frequency of oceanic and continental supershear earthquakes. *Nature Geoscience*, 15(11):942–949, 2022. doi: 10.1038/s41561-022-01055-5.
- Benford, B., DeMets, C., and Calais, E. GPS estimates of microplate motions, northern Caribbean: evidence for a Hispaniola microplate and implications for earthquake hazard. *Geophysical Journal International*, 191(2):481 – 490, 09 2012. doi: 10.1111/j.1365-246x.2012.05662.x.
- Bletery, Q., Sladen, A., Delouis, B., Vallée, M., Nocquet, J.-M., Roland, L., and Jiang, J. A detailed source model for the Mw9.0 Tohoku-Oki earthquake reconciling geodesy, seismology, and tsunami records. *Journal of Geophysical Research: Solid Earth*, 119(10):7636–7653, 2014. doi: 10.1002/2014jb011261.
- Bouchon, M. A simple method to calculate Green's functions for elastic layered media. *Bulletin of the Seismological Society of America*, 71(4):959–971, 1981. doi: 10.1785/bssa0710040959.
- Bouchon, M. and Karabulut, H. The Aftershock Signature of Supershear Earthquakes. *Science*, 320(5881):1323 – 1325, 06 2008. doi: 10.1126/science.1155030.
- Bouchon, M. and Rosakis, A. J. Reply to comment on “How fast is rupture during an earthquake? New insights from the 1999 Turkey earthquakes”. *Geophysical Research Letters*, 29(8): 84–1–84–2, 2002. doi: 10.1029/2002gl015096.
- Bouchon, M., Bouin, M.-P., Karabulut, H., Toksöz, M. N., Dietrich, M., and Rosakis, A. J. How fast is rupture during an earthquake? New insights from the 1999 Turkey Earthquakes. *Geophysical Research Letters*, 28(14):2723–2726, 2001. doi: 10.1029/2001gl013112.
- Bouchon, M., Karabulut, H., Bouin, M.-P., Schmittbuhl, J., Vallée, M., Archuleta, R., Das, S., Renard, F., and Marsan, D. Faulting characteristics of supershear earthquakes. *Tectonophysics*, 493 (3-4):244 – 253, 10 2010. doi: 10.1016/j.tecto.2010.06.011.
- Bowin, C. O. Geophysical study of the Cayman Trough. *Journal of Geophysical Research*, 73(16):5159–5173, 1968. doi: 10.1029/jb073i016p05159.
- Braun, J. J., Mattioli, G. S., Calais, E., Carlson, D., Dixon, T. H., Jackson, M. E., Kursinski, E. R., Mora-Paez, H., Miller, M. M., Pandya, R., Robertson, R., and Wang, G. Focused study of interweaving hazards across the Caribbean. *Eos, Transactions American Geophysical Union*, 93(9):89–90, 02 2012. doi: 10.1029/2012eo090001.
- Burke, K. Tectonic Evolution of the Caribbean. *Annual Review of Earth and Planetary Sciences*, 16(1):201–230, 1988. doi: 10.1146/annurev.ea.16.050188.001221.
- Calais, E. and de Lépinay, B. From transtension to transpression along the northern Caribbean plate boundary off Cuba: implications for the Recent motion of the Caribbean plate. *Tectonophysics*, 186(3-4):329 – 350, 1991. doi: 10.1016/0040-1951(91)90367-2.
- Calais, E., Perrot, J., and de Lépinay, B. Strike-slip tectonics and seismicity along the northern Caribbean plate boundary from Cuba to Hispaniola. In *Special Paper 326: Active Strike-Slip and Collisional Tectonics of the Northern Caribbean Plate Boundary Zone*, volume 326, pages 125 – 169. Geological Society of America, 1998. doi: 10.1130/0-8137-2326-4.125.

- Calais, E., Gonzalez, O., Arango-Arias, E., Moreno, B., Palau, R., Cutie, M., Diez, E., Montenegro, C., Roche, E. R., Garcia, J., Castellanos, E., and Symithe, S. Current deformation along the northern Caribbean plate boundary from GNSS measurements in Cuba. *Tectonophysics*, 868:230068, 2023. doi: 10.1016/j.tecto.2023.230068.
- Cheng, C. and Wang, D. Imaging the rupture process of the 10 January 2018 MW7.5 Swan island, Honduras earthquake. *Earthquake Science*, 33(4):194–200, 2020. doi: 10.29382/eqs-2020-0194-03.
- Delouis, B., Giardini, D., Lundgren, P., and Salichon, J. Joint Inversion of InSAR, GPS, Teleseismic, and Strong-Motion Data for the Spatial and Temporal Distribution of Earthquake Slip: Application to the 1999 Izmit Mainshock. *Bulletin of the Seismological Society of America*, 92(1):278–299, 2002. doi: 10.1785/0120000806.
- deMets, C., Jansma, P. E., Mattioli, G. S., Dixon, T. H., Farina, F., Bingham, R., Calais, E., and Mann, P. GPS constraints on Caribbean-North America plate motion. *Geophysical Research Letters*, 27(3):437–440, 02 2000. doi: 10.1029/1999GL005436.
- Dunham, E. M. Conditions governing the occurrence of supershear ruptures under slip-weakening friction. *Journal of Geophysical Research: Solid Earth*, 112(B7):2006JB004717, July 2007. doi: 10.1029/2006JB004717.
- Dunham, E. M. and Archuleta, R. J. Evidence for a Supershear Transient during the 2002 Denali Fault Earthquake. *Bulletin of the Seismological Society of America*, 94(6B):S256–S268, 2004. doi: 10.1785/0120040616.
- El-Isa, Z. and Eaton, D. W. Spatiotemporal variations in the b-value of earthquake magnitude–frequency distributions: Classification and causes. *Tectonophysics*, 615-616:1–11, 2014. doi: 10.1016/j.tecto.2013.12.001.
- Ellis, A., deMets, C., Briole, P., Cosenza, B., Flores, O., Graham, S. E., Guzmán-Speziale, M., Hernández, D., Kostoglodov, V., LaFemina, P., Lord, N., Lasserre, C., Lyon-Caen, H., Rodriguez Maradiaga, M., McCaffrey, R., Molina, E., Rivera, J., Rogers, R., and Staller, A. GPS constraints on deformation in northern Central America from 1999 to 2017, Part 1 – Time-dependent modelling of large regional earthquakes and their post-seismic effects. *Geophysical Journal International*, 214(3):2177–2194, 2018. doi: 10.1093/gji/ggy249.
- Ellsworth, W. L., Celebi, M., Evans, J. R., Jensen, E. G., Kayen, R., Metz, M. C., Nyman, D. J., Roddick, J. W., Spudich, P., and Stephens, C. D. Near-Field Ground Motion of the 2002 Denali Fault, Alaska, Earthquake Recorded at Pump Station 10. *Earthquake Spectra*, 20(3):597–615, 2004. doi: 10.1193/1.1778172.
- GEBCO. Gridded Bathymetry Data, 2024. https://www.gebco.net/data_and_products/gridded_bathymetry_data/.
- GEOSCOPE. CUBA REGION 2020/01/28 19:10:25 UTC, Mw=7.8, 2021. <http://geoscope.ipgp.fr/index.php/en/catalog/earthquake-description?seis=us60007idc>.
- Graham, S. E., DeMets, C., DeShon, H. R., Rogers, R., Maradiaga, M. R., Strauch, W., Wiese, K., and Hernandez, D. GPS and seismic constraints on the M = 7.3 2009 Swan Islands earthquake: implications for stress changes along the Motagua fault and other nearby faults. *Geophysical Journal International*, 190(3):1625–1639, 2012. doi: 10.1111/j.1365-246x.2012.05560.x.
- Hayman, N. W., Grindlay, N. R., Perfit, M. R., Mann, P., Leroy, S., and de Lépinay, B. Oceanic core complex development at the ultraslow spreading Mid-Cayman Spreading Center. *Geochemistry, Geophysics, Geosystems*, 12(3), 2011. doi: 10.1029/2010gc003240.
- Herring, T. A., King, R. W., Floyd, M., and McClusky, S. C. Introduction to GAMIT/GLOBK, Release 10.6. Technical report, Massachusetts Institute of Technology, 06 2015.
- Holcombe, T. L. and Sharman, G. F. Post-Miocene Cayman Trough evolution: A speculative model. *Geology*, 11(12):714–717, 1983. doi: 10.1130/0091-7613(1983)11<714:pctes>2.0.co;2.
- Hough, S. E., Martin, S. S., Symithe, S. J., and Briggs, R. Rupture Scenarios for the 3 June 1770 Haiti Earthquake. *Bulletin of the Seismological Society of America*, 113(1):157–185, 2023. doi: 10.1785/0120220108.
- Jara, J., Bruhat, L., Thomas, M. Y., Antoine, S. L., Okubo, K., Rougier, E., Rosakis, A. J., Sammis, C. G., Klinger, Y., Jolivet, R., and Bhat, H. S. Signature of transition to supershear rupture speed in the coseismic off-fault damage zone. *Proceedings of the Royal Society A*, 477(2255):20210364, 2021. doi: 10.1098/rspa.2021.0364.
- Johnston, G., Riddell, A., and Hausler, G. The International GNSS Service. In Teunissen, P. and Montenbruck, O., editors, *Springer Handbook of Global Navigation Satellite Systems*. 2017.
- Lapusta, N. and Liu, Y. Three-dimensional boundary integral modeling of spontaneous earthquake sequences and aseismic slip. *Journal of Geophysical Research: Solid Earth*, 114(B9):2008JB005934, Sept. 2009. doi: 10.1029/2008JB005934.
- Lay, T., Kanamori, H., Ammon, C. J., Koper, K. D., Hutko, A. R., Ye, L., Yue, H., and Rushing, T. M. Depth-varying rupture properties of subduction zone megathrust faults. *Journal of Geophysical Research: Solid Earth*, 117(B4), 2012. doi: 10.1029/2011JB009133.
- Leroy, S., de Lépinay, B., Mauffret, A., and Pubellier, M. Structural and Tectonic Evolution of the Eastern Cayman Trough (Caribbean Sea) From Seismic Reflection Data. *American Association of Petroleum Geologists Bulletin*, 80(2):222–247, 1996. doi: 10.1306/64ed8796-1724-11d7-8645000102c1865d.
- Leroy, S., Mauffret, A., Patriat, P., and de Lépinay, B. An alternative interpretation of the Cayman trough evolution from a reidentification of magnetic anomalies. *Geophysical Journal International*, 141(3):539–557, 2000. doi: 10.1046/j.1365-246x.2000.00059.x.
- Mann, P. and Burke, K. Neotectonics of the Caribbean. *Reviews of Geophysics*, 22(4):309–362, 1984. doi: 10.1029/rg022i004p00309.
- Mello, M., Bhat, H., Rosakis, A., and Kanamori, H. Reproducing the supershear portion of the 2002 Denali earthquake rupture in laboratory. *Earth and Planetary Science Letters*, 387:89–96, 2014. doi: 10.1016/j.epsl.2013.11.030.
- Meng, L., Inbal, A., and Ampuero, J.-P. A window into the complexity of the dynamic rupture of the 2011 Mw 9 Tohoku-Oki earthquake: THE 2011 TOHOKU-OKI EARTHQUAKE. *Geophysical Research Letters*, 38(7):n/a–n/a, Apr. 2011. doi: 10.1029/2011GL048118.
- Meng, L., Ampuero, J. P., Sladen, A., and Rendon, H. High-resolution backprojection at regional distance: Application to the Haiti M7.0 earthquake and comparisons with finite source studies. *Journal of Geophysical Research: Solid Earth*, 117(B4):B04313 – 16, 04 2012. doi: 10.1029/2011jb008702.
- Meng, L., Zhang, A., and Yagi, Y. Improving back projection imaging with a novel physics-based aftershock calibration approach: A case study of the 2015 Gorkha earthquake. *Geophysical Research Letters*, 43(2):628–636, 2016. doi: 10.1002/2015gl067034.
- Moreno, B., Grandison, M., and Atakan, K. Crustal velocity model along the southern Cuban margin: implications for the tectonic regime at an active plate boundary. *Geophysical Journal International*, 151:632 – 645, 2002. doi: 10.1046/j.1365-246X.2002.01810.x.
- Moreno, B., Aoudia, A., Manu-Marfo, D., Kherchouche, R., and Pachhai, S. Crust–Uppermost Mantle Structure beneath the Caribbean Region from Seismic Ambient Noise Tomogra-

- phy. *Bulletin of the Seismological Society of America*, 113(3): 1064–1076, 2023. doi: 10.1785/0120220062.
- Nabelek, J. *Determination of earthquake fault parameters from inversion of body waves*. PhD thesis, 1984.
- Peirce, C., Grevemeyer, I., Hayman, N. W., and Van Avendonk, H. J. A. Active ocean–continent transform margins: seismic investigation of the Cayman Trough–Swan Island ridge–transform intersection. *Geophysical Journal International*, 229 (3):1604–1627, 2022. doi: 10.1093/gji/ggac019.
- Perfit, M. R. and Heezen, B. C. The geology and evolution of the Cayman Trench. *Geological Society of America Bulletin*, 89(8):1155 – 21, 1978. doi: 10.1130/0016-7606(1978)89<1155:tgaot>2.0.co;2.
- Perrot, J., Calais, E., and de Lépinay, B. Tectonic and Kinematic Regime along the Northern Caribbean Plate Boundary: New Insights from Broad-band Modeling of the May 25, 1992, Ms = 6.9 Cabo Cruz, Cuba, Earthquake. *Pure and Applied Geophysics*, 149 (3):475 – 487, 06 1997. doi: 10.1007/s000240050036.
- Plafker, G. Tectonic Aspects of the Guatemala Earthquake of 1976 February 1976. *Science*, 193(4259):1201 – 1208, 09 1976. doi: 10.1126/science.193.4259.1201.
- Rosencrantz, E. and Mann, P. SeaMARC II mapping of transform faults in the Cayman Trough, Caribbean Sea. *Geology*, 19(7):690 – 693, 07 1991. doi: 10.1130/0091-7613(1991)019<0690:simotf>2.3.co;2.
- Rosencrantz, E., Ross, M. I., and Sclater, J. G. Age and spreading history of the Cayman Trough as determined from depth, heat flow, and magnetic anomalies. *Journal of Geophysical Research: Solid Earth*, 93(B3):2141 – 2157, 03 1988. doi: 10.1029/jb093ib03p02141.
- Rousseau, C.-E. and Rosakis, A. J. Dynamic path selection along branched faults: Experiments involving sub-Rayleigh and supershear ruptures. *Journal of Geophysical Research: Solid Earth*, 114(B8), 2009. doi: 10.1029/2008jb006173.
- Scholz, C. H. The frequency-magnitude relation of microfracturing in rock and its relation to earthquakes. *Bulletin of the Seismological Society of America*, 58(1):399–415, 1968. doi: 10.1785/bssa0580010399.
- Scholz, C. H. On the stress dependence of the earthquake b value. *Geophysical Research Letters*, 42(5):1399–1402, 2015. doi: 10.1002/2014gl062863.
- Schorlemmer, D., Wiemer, S., and Wyss, M. Variations in earthquake-size distribution across different stress regimes. *Nature*, 437(7058):539 – 542, 09 2005. doi: 10.1038/nature04094.
- Shi, Z. and Ben-Zion, Y. Dynamic rupture on a bimaterial interface governed by slip-weakening friction. *Geophysical Journal International*, 165(2):469–484, 2006. doi: 10.1111/j.1365-246x.2006.02853.x.
- Shlomo, H. and Fineberg, J. The structure of slip-pulses and supershear ruptures driving slip in bimaterial friction. *Nature Communications*, 7(1):11787, 2016. doi: 10.1038/ncomms11787.
- Shlomo, H., Adda-Bedia, M., Arias, R. E., and Fineberg, J. Supershear Frictional Ruptures Along Bimaterial Interfaces. *Journal of Geophysical Research: Solid Earth*, 125(8):e2020JB019829, Aug. 2020. doi: 10.1029/2020JB019829.
- Sylvester, A. G. Strike-slip faults. *GSA Bulletin*, 100(11):1666–1703, 1988. doi: 10.1130/0016-7606(1988)100<1666:ssf>2.3.co;2.
- Symithe, S., Calais, E., Chaballier, J. B., Robertson, R., and Higgins, M. Current block motions and strain accumulation on active faults in the Caribbean. *Journal of Geophysical Research (Solid Earth)*, 120, 2015. doi: 10.1002/2014jb011779.
- Taber, S. The Great Fault Troughs of the Antilles. *The Journal of Geology*, 30(2):89 – 114, 1922. doi: 10.1086/622856;journal:journal;jg;subpage:string:access.
- Tadapansawut, T., Okuwaki, R., Yagi, Y., and Yamashita, S. Rupture Process of the 2020 Caribbean Earthquake Along the Oriente Transform Fault, Involving Supershear Rupture and Geometric Complexity of Fault. *Geophysical Research Letters*, 48(1), 2020. doi: 10.1029/2020gl090899.
- Templeton, E. L., Baudet, A., Bhat, H. S., Dmowska, R., Rice, J. R., Rosakis, A. J., and Rousseau, C.-E. Finite element simulations of dynamic shear rupture experiments and dynamic path selection along kinked and branched faults. *Journal of Geophysical Research: Solid Earth*, 114(B8), 2009. doi: 10.1029/2008jb006174.
- tenBrink, U. S., Coleman, D. F., and Dillon, W. P. The nature of the crust under Cayman Trough from gravity. *Marine and Petroleum Geology*, 19(8):971 – 987, 2002. doi: 10.1016/s0264-8172(02)00132-0.
- tenBrink, U. S., Bakun, W. H., and Flores, C. H. Historical perspective on seismic hazard to Hispaniola and the northeast Caribbean region. *Journal of Geophysical Research: Solid Earth*, 116(B12):B12318 – 15, 12 2011. doi: 10.1029/2011jb008497.
- USGS. M 7.7 - 123 km NNW of Lucea, Jamaica, 2020. <https://earthquake.usgs.gov/earthquakes/eventpage/us60007idc/executive>.
- USGS. M 7.6 - 209 km SSW of George Town, Cayman Islands, 2 2025. <https://earthquake.usgs.gov/earthquakes/eventpage/us7000pcdl/executive>.
- Utsu, T. A method for determining the value of b in the formula $\log n = a - bM$ showing the magnitude-frequency relation for earthquakes. *Geophysical Bulletin of the Hokkaido University*, 13:99–103, 1965.
- vanDusen, S. R. and Doser, D. I. Faulting Processes of Historic (1917–1962) M>6.0 Earthquakes Along the North-central Caribbean Margin. *Pure and Applied Geophysics*, 157(5):719 – 736, 2000. doi: 10.1007/pl00001115.
- Vernant, P. What can we learn from 20 years of interseismic GPS measurements across strike-slip faults? *Tectonophysics*, 644–645(C):22 – 39, 03 2015. doi: 10.1016/j.tecto.2015.01.013.
- Waldhauser, F. HypoDD-A program to compute double-difference hypocenter locations. Technical report, 2001.
- Weertman, J. Subsonic type earthquake dislocation moving at approximately $\sqrt{2}$ x shear wave velocity on interface between half spaces of slightly different elastic constants. *Geophysical Research Letters*, 29(10):109–1–4, 2002. doi: 10.1029/2001GL013916.
- Weng, H. and Ampuero, J.-P. Continuum of earthquake rupture speeds enabled by oblique slip. *Nature Geoscience*, 13(12): 817–821, 2020. doi: 10.1038/s41561-020-00654-4.
- Weng, H., Huang, J., and Yang, H. Barrier-induced supershear ruptures on a slip-weakening fault. *Geophysical Research Letters*, 42(12):4824–4832, June 2015. doi: 10.1002/2015GL064281.
- Wilcox, R. E., Harding, T. P., and Seely, D. R. Basic Wrench Tectonics. *AAPG Bulletin*, 57(1):74–96, 1973. doi: 10.1306/819a424a-16c5-11d7-8645000102c1865d.
- Xu, Z., Sun, L., Rahman, M. N. A., Liang, S., Shi, J., and Li, H. Insights on the Small Tsunami from 28 January 2020 Caribbean Sea MW7.7 Earthquake by Numerical Simulation and Spectral Analysis. *Natural Hazards*, 111:2703–2719, 2022. doi: 10.21203/rs.3.rs-608879/v1.
- Zumberge, J., Heflin, M. B., Watkins, M. M., and Webb, F. H. Precise point positioning for the efficient and robust analysis of GPS data from large networks. *Journal of Geophysical Research (Solid Earth)*, 102(B3):5005–5017, 05 2007. doi:

10.1029/96JB03860.

The article *The 28 January 2020, Mw 7.7, Cayman Trough / Oriente Fault, Supershear Earthquake Rupture* © 2025 by Eric Calais is licensed under CC BY 4.0.